2023 IEEE/ASME International Conference on Advanced Intelligent Mechatronics (AIM)
June 28-30, 2023. Seattle, Washington, USA

Vibration control of semi-active suspension with cam mechanism-based nonlinear stiffness structure

1st Zehua Cai
Engineering College
Ocean University of China
Qingdao, China
caizehua@stu.ouc.edu.cn

2nd Donghong Ning
Engineering College
Ocean University of China
Qingdao, China
ningdonghong@ouc.edu.cn

***Abstract*—This paper proposes a novel semi-active suspension system with a cam mechanism-based nonlinear stiffness structure for vibration reduction. The cam mechanism has a specially designed curve on its contacting surface, which is designed and modeled using the virtual work principle and force-displacement simulation. The nonlinear stiffness structure mainly consists of a spring, a roller and a curved surface. Based on the surface contour design, the system shows variable stiffness characteristics and the required stiffness range can be obtained through the proper design of the curved surface. Then, the model parameters are analyzed, and the key structural parameters of the system are determined to achieve a high-static-low-dynamic stiffness. Additionally, a semi-active backstepping sliding mode controller is designed to enhance the vibration reduction capabilities. Finally, the vibration reduction performance of the passive systems with and without nonlinear stiffness and the semi-active system are compared. The results show both the nonlinear stiffness and the semi-active control are beneficial to reduce vibration. The RMS of acceleration of the nonlinear stiffness passive suspension and semi-active suspension in random excitation decreases 12.9% and 17.2%, respectively.**

Keywords—curved surface design, structural parameters, nonlinear stiffness, vibration reduction, semi-active control

I. INTRODUCTION

In engineering, vibration is inevitable and often leads to detrimental effects. Suspension systems are widely employed across various fields to enhance safety and comfort. On one hand, the linear vibration isolation theory suggests that a suspension can exhibit vibration isolation performance only when the excitation frequency exceeds $\sqrt{2}$ times the natural frequency ($\sqrt{k/m}/(2\pi)$)[1]. Consequently, achieving a lower natural frequency through reduced stiffness is advantageous in vibration reduction. On the other hand, the deformation of the suspension spring is limited by space and stability requirements. Moreover, under a given load, smaller deformations correspond to higher stiffness, which ensures load-bearing capacity. Therefore, suspensions necessitate a delicate balance between stiffness for vibration reduction effect and load-bearing capacity. The contradiction between high load capacity and low natural frequency has posed a challenge in the development of passive vibration isolation technology. Low-frequency vibration isolation, especially for heavy equipment, has remined a persistent challenge[2]. High static stiffness corresponds to a large load-bearing capacity under small deformations, while low dynamic stiffness results in a low natural frequency. The high-static-low-dynamic stiffness (HSLDS) represents a type of nonlinear stiffness that varies with displacement[3]. HSLDS offers a potential solution to the bottleneck problem faced by traditional passive vibration isolation technologies. Various suspensions incorporating nonlinear stiffness have been developed and analyzed previously. For instance, Carrella et al.[4] conducted a comprehensive static analysis of a nonlinear stiffness isolator consisting of a vertical spring and two inclined springs. They investigated the optimal relationship between the spring stiffness ratio and geometric layout[5]. Kovacic et al.[6] replaced linear springs with prestressed nonlinear springs, and further studied the static characteristics of a three-spring nonlinear stiffness isolator. Le et al.[7] devised a nonlinear stiffness isolator by connecting two symmetrical horizontal springs with inclined rods, forming a negative stiffness mechanism that was applied to vehicle seats. Zhou et al.[8] utilized a cam-roller-spring mechanism as a negative stiffness element to construct a quasi-zero stiffness isolator, establishing a piecewise function model. Results indicated that the peak transmissibility and initial isolation frequency of the isolator were lower than those of the corresponding linear system, regardless of the excitation amplitude. Ahn et al.[9] proposed an integrated design method for nonlinear stiffness system and concluded that desired characteristics of a nonlinear stiffness mechanism can be achieved through properly designed cam geometry. In this paper, a new type of nonlinear stiffness suspension with spring-cam-curved surface structure is proposed. By designing the contour of the curved surface, an adjustable force-displacement function can be achieved[10], allowing for the fulfillment of various stiffness requirements, including HSLDS. Theoretical modifications to the curved surface result in nonlinear deformations of the springs, consequently enabling the nonlinear variation of the system's stiffness[11]. The research results hold significant importance for vibration reduction in seats and machinery devices, offering potential improvements in seat comfort and mitigating damage to mechanical components caused by vibration. Moreover, the design of curved surface contours can be tailored to suit other

applications, in accordance with specific usage demands. When combined with appropriate control methods, the proposed suspension system has the potential to further reduce vibrations.

II. Modeling and Analysis

A. Structure and static modeling

This section establishes the static model of the suspension, considering the geometric nonlinearity of the structure, and derives the functional relationship between the load force and displacement. Fig. 1 illustrates the schematic diagram of the nonlinear stiffness suspension. Several key parameters are involved, including the distance l between the installation point of the curved surface structure and the binaural support, the rod length L, the initial stretching length δ_0, and the installation height H of the horizontal spring. Additionally, θ_0 represents the initial inclination angle of the system under no load or only a small load. The spring is pre-stretched, enabling it to possess a certain static load capacity. As the load gradually increases, the force exerted by the curved surface on the cam gradually increases. When it reaches a critical value, the spring separates from the positioning plate. At this point, the spring force solely supports the heavy object and no longer acts on the positioning plate. If the suspension is loaded with a heavy object of gravity mg (mg > the maximum static load), the horizontal spring undergoes further stretching, causing a reduction in the overall height of the system. Consequently, the horizontal spring moves along the curved surface contour to a specific position, attaining a state of equilibrium. The equilibrium position is selected as the location where the dynamic stiffness of the system is minimal. In this way, it can be ensured that the system has a small dynamic stiffness when it moves near the equilibrium position.

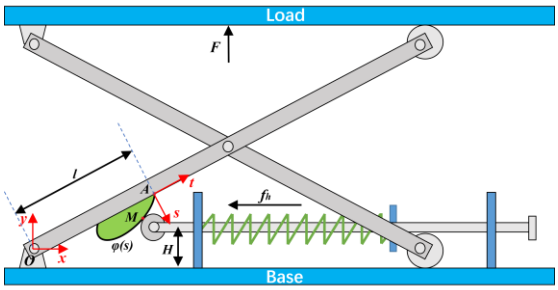

Fig. 1 The schematic diagram of the nonlinear stiffness suspension

The inclination angle between the scissors rod and the horizontal plane is denoted as θ. The curved surface structure is installed at point A, and the t-s coordinate system is established with A as the origin. The curve equation in the t-s coordinate system is represented as $\varphi(s)$, while the contact position of the cam and the surface is identified as point M. Furthermore, a y-x coordinate system is established as shown in Fig.1, with O serving as its origin. The transformation relationship between the curve equation in the two coordinate systems can be derived as follows:

$$\begin{bmatrix} x \\ y \end{bmatrix} = \begin{bmatrix} \cos\left(\frac{\pi}{2}-\theta\right) & \sin\left(\frac{\pi}{2}-\theta\right) \\ -\sin\left(\frac{\pi}{2}-\theta\right) & \cos\left(\frac{\pi}{2}-\theta\right) \end{bmatrix} \begin{bmatrix} s \\ \varphi(s) \end{bmatrix} + \begin{bmatrix} l\cos\theta \\ l\sin\theta \end{bmatrix} \quad (1)$$

The coordinates of the contact point M in the t-s coordinate system are given as (s_M, $\varphi(s_M)$), while the installation height of the spring is denoted as H. Neglecting the impact of the cam size on the contact position, the coordinates of M in the y-x coordinate system can be represented as (x_M, H). By substituting y=H into (1) and incorporating the coordinates of M (s_M, $\varphi(s_M)$), we can establish the relationship between s_M and θ as follows:

$$s_M = f_1(\theta) \quad (2)$$

By substituting (2) into (1), we can express the abscissa x_M of point M in the y-x coordinate system as a function of θ, denoted as:

$$x_M = f_2(\theta) \quad (3)$$

When there is no load, the initial inclination angle of the rod is denoted as θ_0, which is determined by the constant initial height H_0 of the system. Consequently, we can calculate the initial abscissa x_{M_0} of point M in the y-x coordinate system using (3). The deformation Δx of the horizontal spring can be determined by $\Delta x = x_M - x_{M_0}$. The force exerted by the horizontal spring can be expressed as $f_h = k_h(\delta_0 + \Delta x)$, where δ_0 is the pre-stretching amount, k_h is the spring constant. Subsequently, we can establish the relationship between the f_h and θ as follows:

$$f_h = f_3(\theta) \quad (4)$$

For the system composed of the scissors structure, curved surface, cam and springs, the virtual work equation can be expressed as shown in (5). Here we use two springs that are stretched in advance.

$$F \cdot \delta h + 2 f_h \cdot \delta x_M = 0 \quad (5)$$

The ordinate of the plane where the load is equals to the height of the system h, initially set as H_0. It can be represented as $h = Lsin\theta$, and its variation can be described as follows:

$$\delta h = L\cos\theta\delta\theta \quad (6)$$

The abscissa x_M of point M is determined by (3), and its variation can be expressed as follows:

$$\delta x_M = f_2'(\theta)\delta\theta \quad (7)$$

By substituting (6) and (7) into (5), the relationship between load F and rod inclination angle θ can be obtained:

$$F = f_4(\theta) \quad (8)$$

By combining $\theta = \arcsin(h/L)$ and (8), we can obtain:

$$F = f_5(h) \quad (9)$$

B. Design of the contact curved surface

By designing appropriate structural parameters and surface contour, the vibration isolator can exhibit a small dynamic stiffness characteristic near the equilibrium position. The theoretical profile of the curved surface directly determines the deformation of the horizontal springs, which further affects the

stiffness characteristic of the suspension. Fig. 2 shows the primary research route for obtaining the suitable curve function. In this study, the curved surface function is represented solely in polynomial form. Table I presents the main parameters selected for designing the curved surface.

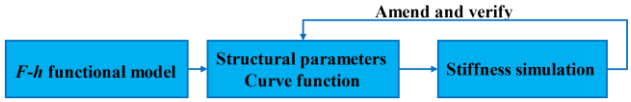

Fig. 2 The prime research route to get proper curve function

TABLE I. MAIN PARAMETERS CHOSEN TO DESIGN CURVED SURFACE

Parameters	Value
Length of the scissors rod L	0.72 m
The initial incline angle of the scissors rod θ_0	π/4 rad
Horizontal spring stiffness k_h	8000 N/m
Distance from the mounting point of the curved surface to the origin of the y-x coordinate	0.32 m
Mounting height of the horizontal springs H	0.20 m
Pre-stretching amount of the horizontal springs δ_0	0.15 m
The balance point below the initial position x_b	0.2681 m
The gravity of the load mg	584.2138 N
The incline angle of the scissors rod θ_b	19.5607°

By utilizing the polynomial block in the Simulink, simulations are conducted based on section A. By comparing the F-h graph, the curve function is determined as (10). The position with the least stiffness is identified as the balance point, as shown in Table I. The displacement from the balance position is defined as $h_b = h - H_0 + x_b$, and the force applied to the suspension is $F_b = mg - F$. By polynomial fitting of the curve using mathematical tools, the mathematical expression of the relationship between F_b and h_b in polynomial form is obtained. Fig. 3 shows the comparison between the exact curve and approximation curves. It can be observed that the stiffness (slope of the F_b-h_b curve) near the equilibrium position is only slightly greater than zero, and the fitting effect improves with increasing polynomial power.

$$\varphi(s) = 38.5s^4 + 13.2s^3 - 0.3s \tag{10}$$

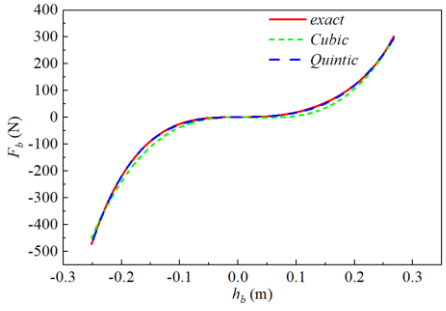

Fig. 3 The exact and fitting curves of force and displacement

Fig. 4 illustrates the force-displacement curves corresponding to different pre-stretching amounts of the springs. It is important to note that the balance position varies with different values of δ_0. Each curve requires a specific load to maintain its own balance position. Moreover, it is observed that certain segments on the curves with δ_0=0.21 and δ_0=0.18 exhibit negative stiffness characteristics. To ensure system stability, it is necessary to eliminate these segments of negative stiffness. Therefore, in our suspension design, we have chosen δ_0 to be 0.15, which fits the system well.

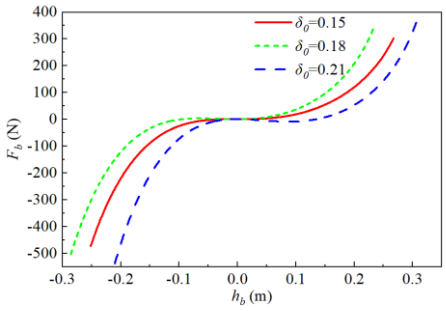

Fig. 4 The force-displacement curves with different δ_0

III. CONTROL

In this section, we have designed a backstepping sliding mode controller and a semi-active strategy to further reduce the vibration in our nonlinear stiffness suspension. The overall technical route of the semi-active control is illustrated in Fig. 5.

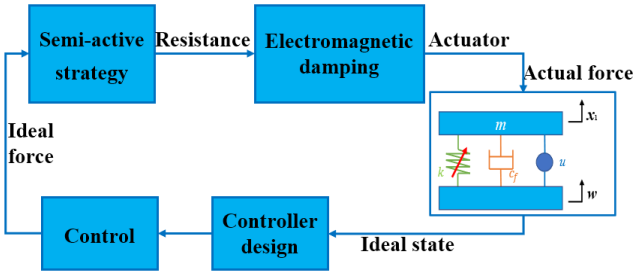

Fig. 5 The overall technical route of semi-active control

A. Controller design

The dynamic function of the suspension with the input u can be described by (11), where m represents the load mass, F_b denotes the applied force, x_1 represents the load's displacement, and w represents the base's displacement. The state-space model of the system can be represented as (12).

$$m\ddot{x}_1 + F_b + c_f\left(\dot{x}_1 - \dot{w}\right) = u \tag{11}$$

$$\begin{cases} \dot{x}_1 = x_2 \\ \dot{x}_2 = -\dfrac{1}{m}\left[F_b + c_f\left(x_2 - \dot{w}\right)\right] + \dfrac{1}{m}u \end{cases} \tag{12}$$

The desired displacement is represented by z_d, and the deviation function is defined as $z_1 = x_1 - z_d$. Considering $V_1 = z_1^2 / 2$ as the candidate Lyapunov function[12], we obtain $\dot{V}_1 = z_1\left(x_2 - \dot{z}_d\right)$. The virtual control input is defined as

$z_2 = x_2 + c_1 z_1 - \dot{z}_d$. Hence, we have $\dot{V}_1 = -c_1 z_1^2 + z_1 z_2$. Here, when z_2 equals to zero, $\dot{V}_1 \le 0$. We define the sliding mode function as s=z_2. The Lyapunov function can be further defined as $V_2 = V_1 + z_2^2 / 2$, and we have $\dot{V}_2 = \dot{V}_1 + z_2 \dot{z}_2$. To ensure $\dot{V}_2 \le 0$ and adopt the reaching law[13], the backstepping sliding mode controller can be designed as (13). We can adopt saturation function 'sat' to replace 'sgn' to eliminate chatter, and the thickness of boundary is Δ. Table II shows the main parameters chosen to design the controller.

$$u(t) = m\left[-\eta \,\mathrm{sgn}(z_2) - c_2 z_2 - c_1 \dot{z}_1 - z_1 + \ddot{z}_d\right] + \left[c_f\left(\dot{x}_1 - \dot{w}\right) + F_b\right] \tag{13}$$

$$\mathrm{sat}(s) = \begin{cases} 1 & s > \Delta \\ ks & |s| \le \Delta \quad k = 1/\Delta \\ -1 & s < -\Delta \end{cases} \tag{14}$$

TABLE II. MAIN PARAMETERS CHOSEN TO DESIGN CONTROLLER

Parameters	Value
Load mass m	59.6 kg
Damping c_f	600 N·s/m
Desired displacement z_d	0 m
Controller parameter c_1	8
Controller parameter c_2	0.5
Controller parameter η	0.02
Thickness of the boundary Δ	0.03

B. Semi-active strategy

Here, electromagnetic damping force is employed for semi-active control. The electromagnetic force acts in the opposite direction to the relative velocity between the load and the base. To achieve effective control, a control logic is required to track the ideal force with the electromagnetic force. The electromagnetic force is generated using a ball screw and a DC motor[14]. The relationship between the electromagnetic force and the current can be described by (15).

$$F = -k_i r_g \cdot i \tag{15}$$

where k_i is the torque constant, r_g is the transmission ratio of the ball screw and can be obtained using $r_g = 2\pi / p$ where p is the pitch of the ball screw. The relationship between the voltage and the relative velocity is as follows:

$$e = k_e \cdot v \tag{16}$$

where k_e is the voltage constant and its relationship with k_i is $k_e = r_g k_i$. The external resistance is R and the internal resistance is r. Then we can calculate the current as follows:

$$i = k_i r_g v / (R + r) \tag{17}$$

According to (15) and (17), the electromagnetic force can be calculated as $F = -(k_i r_g)^2 v / (R + r)$. Then the electromagnetic damping can be obtained by $c_e = (k_i r_g)^2 / (R + r)$. When F and v have the same sign, indicating c_e is negative, we need to set the external resistance to its maximum value in order to achieve minimum damping. This ensures that the difference between the electromagnetic force and the ideal force is minimized. When F and v have different signs, the ideal external resistance is given by (18). By adjusting the external resistance R_e as close as possible to R, we can achieve an actual control force that is close to the ideal force[15]. Table III presents the parameters of the DC motor.

$$R = -(k_i r_g)^2 v / F - r \tag{18}$$

TABLE III. MAIN PARAMETERS OF THE DC MOTOR

Parameters	Value
The pitch of the ball screw p	0.02 m
Torque constant k_i	0.245 N·m/A
Internal resistance of the motor r	1.6 Ω

IV. VIBRATION RESPONSE ANALYSIS AND COMPARISON

In this section, we compare the vibration responses of three systems: the passive system with contact curved surface (legend 'PS(CV)'), and passive system without contact curved surface (legend 'PS(NCV)'), and the semi-active system with contact curved surface (legend 'SA(CV)'). We examine their responses under three different excitations. To ensure a reliable comparison, we introduce a passive system with the same static displacement under the load mg but without a contact curved surface. The stiffness of PS(NCV) can be obtained by $k_p = mg / x_b$. All three systems are implemented in Simulink for analysis and comparison.

A. Sinusoidal excitation

The vibration performance of the systems is tested using a sinusoidal excitation with the $w = w_0 \sin(2\pi f t)$. The excitation frequency f and amplitude w_0 are set to 1.2Hz and 0.012m, respectively. The acceleration and displacement responses of the three systems are presented in Fig. 6 and Fig. 7. It can be observed that the curved surface design has a positive impact on vibration isolation, and the semi-active control further reduces the vibration. Compared to the PS (NCV) system, the peak acceleration has been reduced by 29.8% and 33.3% in the PS(CV) and SA(CV), respectively. Similarly, the maximum displacement has been reduced by 27.5% and 35.9%, respectively. Fig. 8 illustrates the semi-active electromagnetic force that tracks the ideal force, along with the corresponding resistance used to achieve the tracking. Due to the discontinuity of the actual force, it is impossible to track the ideal force completely.

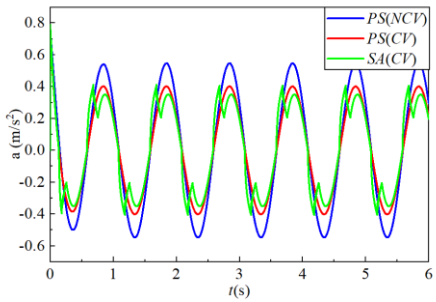

Fig. 6 The acceleration response under sine wave input

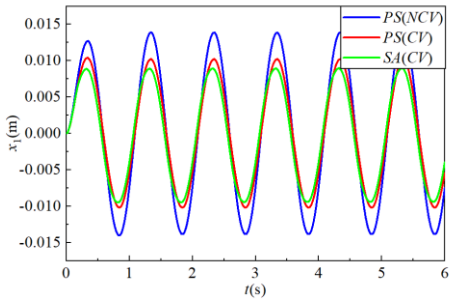

Fig. 7 The displacement response under sine wave input

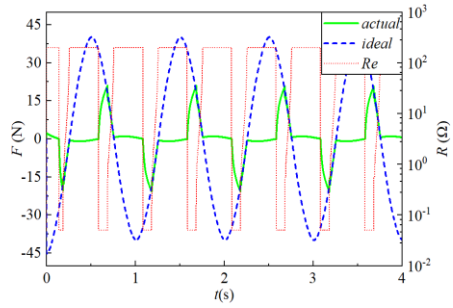

Fig. 8 The force tracking and resistance adopted under sine wave input

B. *Bump excitation*

The bump input applied to the three systems is as follows:

$$w=\begin{cases}0.012(1-\cos(4\pi t)) & (0\le t\le 0.5)\\ 0 & (t\ge 0.5)\end{cases} \tag{19}$$

Fig. 9 and Fig. 10 displays the comparison curves of acceleration and displacement, respectively under bump excitation. When equipped with a curved surface, the peak value of acceleration decreases by a maximum of 23.8%. Furthermore, with the application of semi-active control, the peak value reduces even further by 10.1%. Fig. 11 illustrates the actual force tracking the ideal force, which cannot be achieved completely due to the discontinuity of the external resistance. The figure also presents the current generated in the DC motor. Initially, the current is positive and later switches to negative, indicating a change in relative velocity from positive to negative. Since the ideal force and relative velocity have the same direction segments, the external resistance needs to be set to the maximum value, causing the actual force to track the ideal force for only a brief period of time.

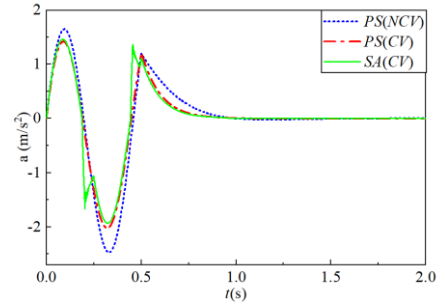

Fig. 9 The acceleration response under bump input

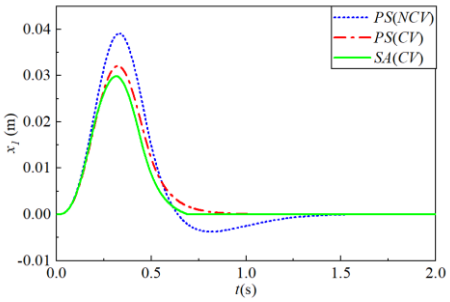

Fig. 10 The displacement response under bump input

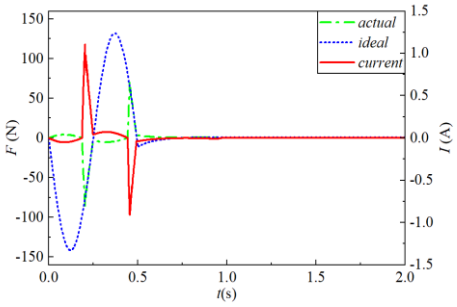

Fig. 11 The force tracking and current generated under bump input

C. *Random excitation*

The random road profile can be generated using (20), where N is the number of the data points to be generated; Δn is the interval of spatial frequency; n_0=0.1 cycles/m is a predefined spatial frequency in ISO 8608; φ_i represents the random phase angle, ranging from 0 to 2π; x is the abscissa variable from 0 to the length of the road; k is a constant ranging from 3 to 9, which is related to the road profile class.

$$h(x)=\sum_{i=1}^{N}2^{k}\sqrt{\Delta n}\cdot 10^{-3}\left(\frac{n_0}{i\cdot\Delta n}\right)\cos\left(2\pi i\cdot\Delta n\cdot x+\varphi_i\right) \tag{20}$$

The road profile is input into a vehicle suspension model, resulting in a random signal. Fig. 12 shows the road profile and the random signal applied to the suspensions. Fig. 13 and Fig. 14 show the acceleration and displacement responses to the random input. When compared to the PS(NCV), the SA(CV) and PS(CV) systems reduce the RMS of acceleration by 17.2% and 12.9%, respectively. Fig. 15 shows the amplitude-frequency characteristics under random excitation, indicating that the SA(CV) system exhibits smaller amplitudes in the low-frequency range compared to the other two systems.

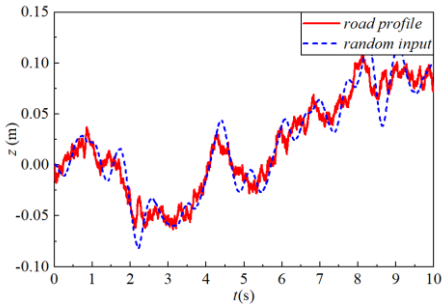

Fig. 12 The road profile and the random signal generated

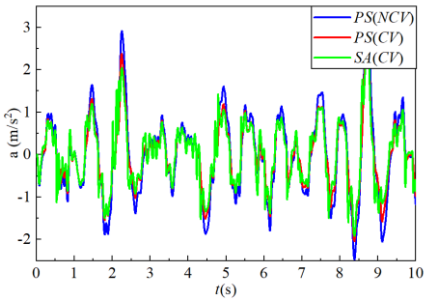

Fig. 13 The acceleration response under random input

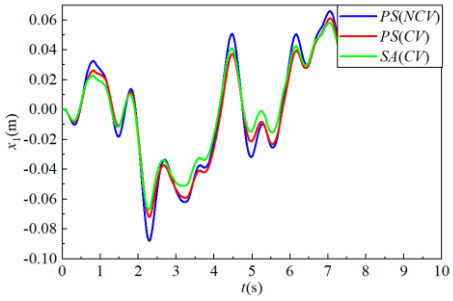

Fig. 14 The displacement response under random input

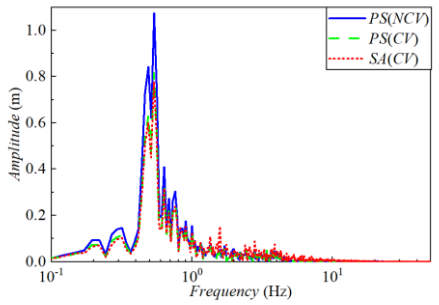

Fig. 15 The amplitude-frequency characteristic under random input

V. Conclusion

In this paper, a semi-active suspension with a nonlinear stiffness structure has been designed and modeled. A backstepping sliding mode controller has been applied to the model to reduce vibration. As a result, the following conclusions can be drawn:

(1) Proper design of the curved surface allows for achieving high static and low dynamic stiffness.

(2) A comparison between the passive system with and without the nonlinear stiffness structure reveals that the design is beneficial for vibration reduction. The system exhibits smaller displacements and can reduce the peak acceleration values by 29.8% and 23.8% under sinusoidal excitation and bump excitation, respectively, as demonstrated in this paper. Furthermore, under random excitation, the RMS of acceleration is reduced by 12.9% and 17.2% for PS (CV) and SA (CV) systems, respectively, as reported in this paper.

Acknowledgment

This research was funded by the National Natural Science Foundation of China (Grant No. 52088102) and the Nature Science Foundation of Shandong (Grant No. 2022HWYQ-067).

References

[1] B. Garnier, B. P. Dupuy, and C. Clerc, "Vibration isolation and damping solutions for space structures," 2022.

[2] C. H. Lu, H. B. J. J. o. V. Bai, and Shock, "A new type nonlinear ultra-low frequency passive vibration isolation system," vol. 30, no. 1, pp. 234-236, 2011.

[3] A. J. U. o. S. Carrella, "Passive vibration isolators with high-static-low-dynamic-stiffness," 2008.

[4] A. Carrella, M. J. Brennan, T. P. J. J. o. S. Waters, and Vibration, "Static analysis of a passive vibration isolator with quasi-zero-stiffness characteristic," vol. 301, no. 3-5, pp. 678-689, 2007.

[5] A. Carrella, M. J. Brennan, T. P. J. J. o. M. S. Waters, and Technology, "Optimization of a quasi-zero-stiffness isolator," vol. 21, no. 6, pp. 946-949, 2007.

[6] I. Kovacic, M. J. Brennan, T. P. J. J. o. S. Waters, and Vibration, "A study of a nonlinear vibration isolator with a quasi-zero stiffness characteristic," no. 3, p. 315, 2008.

[7] T. D. Le, K. K. J. J. o. S. Ahn, and Vibration, "A vibration isolation system in low frequency excitation region using negative stiffness structure for vehicle seat," vol. 330, no. 26, pp. 6311-6335, 2011.

[8] J. Zhou, X. Wang, D. Xu, and S. Bishop, "Nonlinear dynamic characteristics of a quasi-zero stiffness vibration isolator with cam–roller–spring mechanisms," *Journal of Sound and Vibration,* vol. 346, pp. 53-69, 2015.

[9] H.-J. Ahn, S.-H. Lim, and C. Park, "An integrated design of quasi-zero stiffness mechanism," *Journal of Mechanical Science and Technology,* vol. 30, no. 3, pp. 1071-1075, 2016.

[10] S. Wang and Z. Wang, "Curved surface-based vibration isolation mechanism with designable stiffness: Modeling, simulation, and applications," *Mechanical Systems and Signal Processing,* vol. 181, 2022.

[11] H. Junshu, M. Lingshuai, and S. Jinggong, "Design and Characteristics Analysis of a Nonlinear Isolator Using a Curved-Mount-Spring-Roller Mechanism as Negative Stiffness Element," *Mathematical Problems in Engineering,* vol. 2018, pp. 1-15, 2018.

[12] K. E. Majdoub, F. Giri, and F. Z. J. I. C. J. o. A. S. Chaoui, "ADAPTIVE BACKSTEPPING CONTROL DESIGN FOR SEMI-ACTIVE SUSPENSION OF HALF-VEHICLE MR DAMPER," vol. 8, no. 3, pp. 582-596, 2022.

[13] O. Boughazi, A. Boumedienne, and H. Glaoui, "Backstepping Sliding Mode Control," 2015.

[14] P. Liu, M. Zheng, D. Ning, N. Zhang, H. J. M. S. Du, and S. Processing, "Decoupling vibration control of a semi-active electrically interconnected suspension based on mechanical hardware-in-the-loop," vol. 166, pp. 108455-, 2022.

[15] D. Ning, H. Du, S. Sun, W. Li, and W. Li, "An Energy Saving Variable Damping Seat Suspension System With Regeneration Capability," *IEEE Transactions on Industrial Electronics,* vol. 65, no. 10, pp. 8080-8091, 2018.